



HAL
open science

Weakly monotone finite volume scheme for parabolic equations in strongly anisotropic media

Moha Aberrah, El Houssaine Quenjel, Patrick Perré, Mohamed Rhoudaf

► **To cite this version:**

Moha Aberrah, El Houssaine Quenjel, Patrick Perré, Mohamed Rhoudaf. Weakly monotone finite volume scheme for parabolic equations in strongly anisotropic media. *Journal of Applied Mathematics and Computing*, 2023, 69 (4), pp.3289-3316. 10.1007/s12190-023-01883-7. hal-04452270

HAL Id: hal-04452270

<https://hal.science/hal-04452270>

Submitted on 12 Feb 2024

HAL is a multi-disciplinary open access archive for the deposit and dissemination of scientific research documents, whether they are published or not. The documents may come from teaching and research institutions in France or abroad, or from public or private research centers.

L'archive ouverte pluridisciplinaire **HAL**, est destinée au dépôt et à la diffusion de documents scientifiques de niveau recherche, publiés ou non, émanant des établissements d'enseignement et de recherche français ou étrangers, des laboratoires publics ou privés.

Weakly monotone finite volume scheme for parabolic equations in strongly anisotropic media

Moha Aberrah¹, El Houssaine Quenjel², Patrick Perré², and Mohamed Rhoudaf¹

¹Moulay Ismaïl University, Faculty of Sciences, B.P. 11201 Zitoune 50 500 Meknès, Morocco.
moha.aberrah@edu.umi.ac.ma, m.rhoudaf@umi.ac.ma

²Université Paris-Saclay, CentraleSupélec, Laboratoire de Génie des Procédés et Matériaux,
Centre Européen de Biotechnologie et de Bioéconomie (CEBB), 3 rue des Rouges Terres
51110 Pomacle, France. el-houssaine.quenjel@centralesupelec.fr,
patrick.perre@centralesupelec.fr

October 4, 2023

Abstract

In this work, we propose an original idea consisting of preserving the weak monotonicity of the CVFE scheme, or generally for schemes written under the two-point like formulation. The setting handles highly anisotropic and heterogeneous diffusion tensors. The key idea is to insert a nonlinear correcting coefficient whose objective is to eliminate the anti-diffusive fluxes. This modification works on the same stencil as the initial discretization. The obtained scheme remains stable in the sense that the solution respects its physical ranges and enables the energy estimates. The existence of discrete solutions is also valid. The numerical section highlights the accuracy, the robustness and the efficiency of the novel scheme compared to the standard CVFE methodology. An application of the developed weakly monotone finite volume scheme to the simulation of mass transfer in hygroscopic media is conducted, with a specific focus on mass diffusion within wood.

Keywords: finite volumes, monotonicity, parabolic equation, anisotropy, mass transfer, wood.

AMS subject classifications: 74S10, 35K55, 35B50, 80A20.

1 Introduction

Parabolic equations are involved in many physical and biological processes. For example, they are part of complex systems such as flows in porous media,

models of computational fluid dynamics and problems of mass and heat transfer. Bringing new methods of the resolution preserving the scheme's stability and the good behavior of the numerical solutions is of chief importance for practical applications.

Finite volumes [19] and finite elements [17] or more generally the gradient discretization methods [16] are the most popular discrete variational methods widely used for discretizing diffusion problems in space. They are constructed based on two fundamental stability points of type energy estimates and consistency. The latter consists in the convergence of the discrete operators such the gradient and the fluxes towards their continuous counterparts. Depending on the location of the primary unknowns and the construction of the discrete gradient or fluxes, many methods have been developed in the literature. For instance let us cite Two-Point Flux Approximation (TPFA) [21, 20] schemes, Multi-Point Flux Approximation (MPFA) schemes [1, 2], the DDFV methods [5, 6, 14, 30], the vertex approximation gradient approach (VAG) [8, 22, 7], the HMM methods [12]. A general description of weak and strength points of each method can be found in [15]. However, when it comes to the discrete maximum principle, only a couple of methods are fulfilling this property as witnessed in the benchmark [29]. This the case of the TPFA methods or the CVFE schemes [3, 24, 25]. The price to pay is of course restrictive assumptions on the mesh to be orthogonal or the angle condition in the case of simplicial meshes.

Some recent works focused on the positivity of the scheme which is less demanding than monotonicity [11, 26, 27, 28, 38, 39, 41]. The main idea is to make use of the model degeneracy or some singular logarithmic functionals to reinforce this feature. Such techniques are suitable and applied to the context of complex flows in porous media or systems of chemotaxis [8, 31]. This idea is no longer valid if one wants the numerical solution to be bigger than a tough initial condition including a ramp for instance. To deal with such a circumstance, we are led to develop advanced corrections of the problematic fluxes. Before that, let us mention that there exist already several nonlinear monotone schemes in the literature, see for instance [9, 10, 13, 33, 32, 34, 35, 42, 43]. Their stencil construction resembles to the two-point formalism or a contained multi-point structure. However, the stencil includes additional neighbor unknowns and may become very demanding. This is very difficult to apply for complex flows in porous media for instance.

The current contribution brings a new insight on how to construct finite volume schemes respecting the weak monotonicity of the solution. This class of schemes is referred to as weakly monotone finite volumes (WMFV). In other words, formally, if the initial condition (the solution at $t = 0$) is bigger than a given function $x \rightarrow g(x)$, the numerical solution remains also greater than g . This is presented in the context of the CVFE scheme for parabolic equation. This theory is validated through a series of numerical tests. They reveal that the accuracy of the WMFV method is similar to the standard CVFE approach. An application to the simulation of mass transfer in hygroscopic media is provided. We have chosen the example of wood for its a high ratio of anisotropy.

The assets of the present work are summarized in the following list.

- Ensure the weak monotonicity of the numerical solution.
- Keep the same stencil as the initial scheme.
- Maintain the numerical second order accuracy (when the solution is smooth).
- Handle general triangular meshes.
- Deal with highly anisotropic and heterogeneous tensors.

The rest of the paper is articulated as follows. In section 2, we sketch the mathematical model and the main assumptions on the data set and the nonlinearities. Section 3 is devoted to the mesh description as well as the finite element finite volume setting. In Section 4, we present the finite volume discretization and show how to incorporate a nonlinear damping parameter used to reinforce the weak monotonicity of the scheme. Then, one performs the numerical analysis of the method. Section 5 is divided into two parts. The first one aims to the validation of the proposed WMFV scheme, assesses its accuracy and compare it to the standard CVFE approximation. The second part applies the novel methodology to the simulation of mass transfer through hygroscopic media of the wood type. Section 6 concludes the paper and underlines some perspectives of great importance.

2 Problem model

The aim of this paper is to devise and study properties of a new weak monotone finite volume discretization for parabolic equation.

Let $t_f \geq 0$ account for time, the problem is considered in $Q_{t_f} = \Omega \times (0, t_f)$ where Ω is a polygonal connected open bounded subset of \mathbb{R}^d ($d \geq 2$). We denote by $\partial\Omega$ the boundary of Ω and \mathbf{n} the outward normal vector to $\partial\Omega$. Note that the boundary $\partial\Omega$ is divided into parts i.e $\partial\Omega = \partial\Omega^D \cup \partial\Omega^N$. Dirichlet's (resp. Neumann's) boundary is denoted by the superscript D (resp. N). The equation model we are concerned with is written under the form

$$\begin{cases} \phi u_t - \operatorname{div}(\eta(u)\Lambda\nabla u) = f & \text{in } Q_{t_f}, \\ u(0, \cdot) = u^0 & \text{in } \Omega, \\ u = 0 & \text{on } \partial\Omega^D, \\ (\eta(u)\Lambda\nabla u) \cdot \mathbf{n} = 0 & \text{on } \partial\Omega^N \times (0, t_f), \end{cases} \quad (1)$$

where the main unknown is u . Depending on the application, u may stand for the water content, saturation or density of physical quantity. The following assumptions prescribed on the data and on the nonlinearities are classical for the mathematical study of the problem.

(H₁) The initial condition u^0 is considered to be in $L^2(\Omega)$. Assume that $u^0 \geq g \geq 0$ for a given $g \in L^2(\Omega)$.

(H₂) The porosity ϕ is an L^∞ -function and there exist two positive constants ϕ_0 and ϕ_1 such that $\phi_0 \leq \phi \leq \phi_1$.

(H₃) The diffusion (permeability) tensor Λ belongs to $(L^\infty(\Omega))^{d \times d}$, and it is assumed to be symmetric and uniformly elliptic within Ω , meaning that there exist two positive constants $\underline{\Lambda}$ and $\bar{\Lambda}$ such that

$$\underline{\Lambda}|\mathbf{v}|^2 \leq \Lambda(x)\mathbf{v} \cdot \mathbf{v} \leq \bar{\Lambda}|\mathbf{v}|^2, \quad \forall \mathbf{v} \in \mathbb{R}^d \quad \text{for a.e. } x \in \Omega.$$

(H₄) The mobility function $\eta : [0, +\infty) \rightarrow \mathbb{R}^+$ is assumed to be continuous and nondecreasing.

(H₅) The second member f is nonnegative and belongs to $L^2(Q_{t_f})$.

In order to give a mathematical significance to the solution of (1), we are led to introduce a central functional referred to as Kirchhoff's transform $\xi : \mathbb{R}^+ \rightarrow \mathbb{R}^+$, defined by

$$\xi(u) = \int_0^u \sqrt{\eta(s)} ds. \quad (2)$$

The functional framework in which we look for solutions in the weak sense for the continuous problem (1) involves the classical Sobolev space

$$H_D^1(\Omega) = \{u \in H^1(\Omega) / u = 0 \text{ on } \partial\Omega^D\}.$$

(H₆) There exist $C_\xi, C'_\xi > 0$ such that ξ fulfills

$$C_\xi|a| \leq C'_\xi + |\xi(a)|, \quad \forall a \in \mathbb{R}. \quad (3)$$

Moreover, $H_D^1(\Omega)$ is a Hilbert space endowed with the norm

$$\|u\|_{H_D^1(\Omega)} = \|\nabla u\|_{L^2(\Omega)^d}.$$

Remark 1. • *Contrary to some previous works [11, 28, 37], we do not impose here the degeneracy of η i.e., $\eta(0) = 0$ so that the solution can obey its physical ranges. Our work is free of this restriction.*

- *Note that the product of η and Λ can be replaced with a more general nonlinear diffusion tensor of the form $\Lambda(x, \cdot)$ such that: (i) $x \rightarrow \Lambda(x, \cdot)$ is measurable and uniformly elliptic ; (ii) $s \rightarrow \Lambda(\cdot, s)$ is continuous and nondecreasing.*

Definition 1. *Under Assumptions (H₁)-(H₆), a measurable function $u : Q_{t_f} \rightarrow \mathbb{R}$ is said to be a weak solution of (1) if $\xi(u) \in L^2((0, t_f); H_D^1(\Omega))$, and for all $\psi \in C_c^\infty(Q_{t_f})$ one has*

$$-\int_\Omega \phi u^0 \psi(x, 0) dx - \int_{Q_{t_f}} \phi u \psi_t \, dx \, dt + \int_{Q_{t_f}} \sqrt{\eta(u)} \Lambda \nabla \xi(u) \cdot \nabla \psi \, dx \, dt = \int_{Q_{t_f}} f \psi \, dx \, dt. \quad (4)$$

Theorem 1. *The problem (1) has a unique weak solution in the sense of Definition 1.*

Proof. For the existence of a weak solution to the problem (1), we refer to this paper [4] and to the work [36] for the uniqueness. \square

3 CVFE discrete setting

The numerical resolution of the main problem (1) requires the introduction of two different discretizations of the domain Ω , namely a primal mesh and the corresponding dual mesh.

The primal mesh \mathcal{T} is a conforming triangulation of the domain Ω in the sense of the finite elements, consisting of a finite number of triangles which is a partition of the domain Ω i.e., $\bar{\Omega} = \bigcup_{T \in \mathcal{T}} \bar{T}$ et $T \cap T' = \emptyset$ if $T \neq T'$. For each triangle $T \in \Omega$, we denote by x_T its barycenter T , h_T its diameter, and $|T|$ its Lebesgue measure. The set of vertices of \mathcal{T} (resp $T \in \mathcal{T}$) is denoted by \mathcal{V} (resp \mathcal{V}_T). The external vertices belonging to Dirichlet's boundary are given by the set \mathcal{V}^D . For each vertex $K \in \mathcal{V}$, we define T_K the set of triangles which share the vertex K .

Let ρ_T be the diameter of the largest ball included in the triangle T . The size and the regularity of the triangulation \mathcal{T} are respectively denoted by $h_{\mathcal{T}}$ and $\theta_{\mathcal{T}}$ and they are defined by

$$h_{\mathcal{T}} := \max_{T \in \mathcal{T}} (h_T), \quad \theta_{\mathcal{T}} := \max_{T \in \mathcal{T}} \frac{h_T}{\rho_T}.$$

The aim of the CVFE method is to reconstruct the approximate solution at the vertices of the primal mesh following the finite volume spirits. To do this, a new partition of the domain is defined so that each vertex of the primal mesh is uniquely associated to a control volume. The resulting mesh from this second partition is called dual mesh denoted by \mathcal{D} . The cell $A_K \in \mathcal{D}$ is defined by connecting the barycenter of each triangle of T_K with the midpoint of edges having K as an extremity. The center of A_K is the vertex x_K and its surface is denoted by $|A_K|$. Let $T \in T_K$, for $K \neq L \in \mathcal{V}_T$, we define the segment $\sigma_{KL}^T = \partial \bar{K} \cap \partial \bar{L} \cap \bar{T}$. Each interface σ_{KL}^T is characterized by its length $|\sigma_{KL}^T|$ and the unit normal $n_{\sigma_{KL}^T}^T$ oriented from K to L . We designate by $\mathcal{E}_{\mathcal{T}}^*$ the dual edges of \mathcal{D} included in the triangle $T \in \mathcal{T}$.

An illustration of primal triangular and dual meshes is plotted on Figure 1.

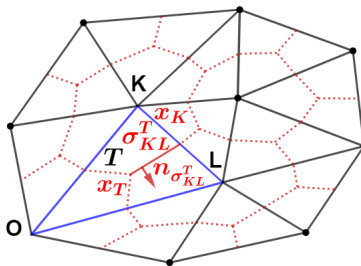


Figure 1: triangular mesh \mathcal{T} (continuous lines) and the corresponding dual mesh \mathcal{D} (dashed lines).

Given $K \in \mathcal{V} \setminus \mathcal{V}^D$ we consider u_K the CVFE approximation of $u(x_K)$. Thus, the discrete unknowns will be denoted by $\{u_K\}_{K \in \mathcal{V}}$.

Next, we define the following finite dimensional space:

$$\mathcal{H}_{\mathcal{T}} = \{\Phi \in H^1(\Omega) \mid \Phi|_T \text{ is affine, } \forall T \in \mathcal{T}\}.$$

The basis of $\mathcal{H}_{\mathcal{T}}$ is spanned by the shape functions $(\varphi_K)_{K \in \mathcal{V}}$ such that $\varphi_K(x_L) = \delta_{KL}$ for all $L \in \mathcal{V}$, δ_{KL} being the Kronecker symbol, every function $s_{\mathcal{T}} \in \mathcal{H}_{\mathcal{T}}$ writes:

$$s_{\mathcal{T}} = \sum_{K \in \mathcal{V}} s_K \varphi_K.$$

And its corresponding discrete gradient is defined as follows

$$\nabla s_{\mathcal{T}} = \sum_{K \in \mathcal{V}} s_K \nabla \varphi_K.$$

On the other hand, we define the trial space $X_{\mathcal{D}}$ of the piecewise constant functions on the dual mesh \mathcal{D} by:

$$X_{\mathcal{D}} = \{\Phi : \Omega \rightarrow \overline{\mathbb{R}} \text{ measurable} \mid \Phi|_{A_K} \in \overline{\mathbb{R}} \text{ is constant } \forall K \in \mathcal{V}\}.$$

For the time discretization, it is given by a strictly increasing sequence of real numbers (t^n) for $n = 0, \dots, n_f$ such that

$$t^0 = 0 < t^1 < \dots < t^{n_f-1} < t^{n_f} = t_f.$$

The size of the time sub-interval is denoted by $\delta t^n = t^{n+1} - t^n$, for $n = 0, \dots, n_f - 1$, and $\delta t = \max_{n=0, \dots, n_f} \delta t^n$. To simplify the notations, we consider a constant time stepping i.e., $\delta t = \delta t^n$ for every $n \in \{0, \dots, n_f - 1\}$.

Let us introduce the transmissibility coefficient between K and L in T

$$\Lambda_{KL}^T = - \int_T \Lambda \nabla \varphi_K(x) \cdot \nabla \varphi_L(x) dx = \Lambda_{LK}^T \in \mathbb{R}. \quad (5)$$

In the following lemma, the formula of the discrete integration by parts is recalled. Its proof can be documented in [11].

Lemma 2. *Let $s_{\mathcal{T}}, \psi_{\mathcal{T}} \in \mathcal{H}_{\mathcal{T}}$, then*

$$\int_{\Omega} \Lambda \nabla s_{\mathcal{T}} \cdot \nabla \psi_{\mathcal{T}} dx = \sum_{T \in \mathcal{T}} \sum_{\sigma_{KL}^T \in \mathcal{E}_T^*} \Lambda_{KL}^T (s_K - s_L) (\psi_K - \psi_L). \quad (6)$$

Consider the right hand side $f \geq 0$. Let (u_K^n) a finite volume solution approximating the weak solution to the continuous problem (1). The corresponding numerical scheme is called:

- (i) positive if $u_K^0 > 0$ implies $u_K^{n+1} > 0$, for all K and n ;
- (ii) minimum-preserving if $u_K^0 > a$ implies $u_K^{n+1} > a$, for some scalar $a \geq 0$;
- (iii) monotone if $u_K^0 > v(x)$ implies $u_K^{n+1} > v(x)$, for some function $v \geq 0$;

By default, the following assertion holds true

$$(iii) \implies (ii) \implies (i).$$

Throughout this work, we are going to build a new finite volume method satisfying a weaker monotone property i.e. between (ii) and (iii) because the scheme depends on the ranges of the initial datum specified by the function g mentioned in Assumption (\mathbf{H}_1) . As a consequence, the weakly monotone scheme is only positive but also preserves the minimum principle. However, the inverse is false in general. Examples are given in the numerical section to highlight this fact. When the scheme is fulfilling one of the aforementioned properties, we say that it verifies the discrete maximum principle.

4 Weakly monotone finite volume scheme and its properties

In this section, we elaborate the weakly monotone finite volume scheme and study some of its theoretical properties, notably stability and existence results. The presentation of the method is done in 2D, but extensions to 3D are naturally possible, see for instance [28].

4.1 Numerical scheme

The CVFE approach is a class of the finite volume methods where the gradient is constructed on the triangles in the sense of finite elements. The fully implicit discretization in time is considered in order to prevent restrictions on the time stepping in case of strong anisotropy or tough initial conditions. As a result, the scheme is essentially derived by integrating the equation (1) over each $A_K \times (t^n, t^{n+1})$. Then, using the Green formula for the divergence integral, we obtain

$$\int_{t^n}^{t^{n+1}} \int_{A_K} \phi u_t dx dt - \sum_{\sigma \in \mathcal{E}_K} \int_{t^n}^{t^{n+1}} \int_{\sigma} \eta(u) \Lambda \nabla u \cdot n_{\sigma} d\sigma dt = \int_{t^n}^{t^{n+1}} \int_{A_K} f dx dt, \quad (7)$$

where n_{σ} is the unit normal pointing outwards A_K . The evolution term is approximated thanks to the first order Euler scheme

$$\int_{t^n}^{t^{n+1}} \int_{A_K} \phi u_t dx dt \approx |A_K| \phi_K (u_K^{n+1} - u_K^n).$$

In the CVFE setting, the diffusion part is commonly discretized as follows

$$- \sum_{\sigma \in \mathcal{E}_K} \int_{t^n}^{t^{n+1}} \int_{\sigma} \eta(u) \Lambda \nabla u \cdot n_{\sigma, K} d\sigma dt \approx \delta t \sum_{T \in \mathcal{T}_K} \sum_{L \in \mathcal{V}_T \setminus \{K\}} \eta_{KL}^{n+1} \Lambda_{KL}^T (u_K^{n+1} - u_L^{n+1}),$$

where the choice of the nonlinear diffusion coefficient η_{KL}^{n+1} is crucial and determinant. In our recent work, and the references are therein, [28] we proposed and studied some formulas of η_{KL}^{n+1} with pros and cons in terms of accuracy and stability. Nevertheless, all these propositions yield only to positive solutions, which is not sufficient in some practical applications in complex flows in porous media or heat transfer in hygroscopic media.

In the present contribution, we elaborate a new formulation of the underlined coefficient with better and strong properties in terms of the discrete maximum principle as well as enjoying an easy numerical implementation. The main idea is to consider a centered approximation of η_{KL}^{n+1} under the form

$$\eta_{KL}^{n+1} = \eta_T^{n+1} \beta_{KL}^{n+1}, \quad (8)$$

where

$$\eta_T^{n+1} = \frac{1}{\#\mathcal{V}_T} \sum_{K \in \mathcal{V}_T} \eta(u_K^{n+1}).$$

The originality consists in introducing the particular nonlinear parameter β_{KL}^{n+1} such that

$$\beta_{KL}^{n+1} = \begin{cases} 1 & \text{if } \Lambda_{KL}^T \geq 0, \\ \beta(u_K^{n+1} - g_K) \beta(u_L^{n+1} - g_L), & \text{if } \Lambda_{KL}^T < 0. \end{cases}$$

where

$$\beta(a) = 1 - \exp\left(\frac{-\max(a, 0)^2}{2\gamma_T^2}\right), \quad \forall a \in \mathbb{R}. \quad (9)$$

Here the function g is given. It was specified in Assumption (**H**₁). It is generally linked to the initial solution. Observe that $\beta_{KL}^{n+1} = \beta_{LK}^{n+1}$, which maintains the flux conservation property of the numerical scheme. The parameter $\gamma_T > 0$ is of great importance in controlling the additional artificial viscosity and therefore the accuracy. Its choice will be discussed later on in the numerical section.

The right hand side f is approximated using the mean value over the control volume A_K .

So, the weakly monotone finite volume scheme that we propose for the discretization of the parabolic problem (1) is given by the following discrete system. The initial condition is approximated by

$$u_K^0 = \frac{1}{|A_K|} \int_{A_K} u^0(x) dx, \quad \forall K \in \mathcal{V} \setminus \mathcal{V}^D, \quad u_K^0 = 0, \quad \forall K \in \mathcal{V}^D. \quad (10)$$

Then, at each time level $n \in \{0, \dots, n_f - 1\}$ the balance equation writes

$$\phi_K(u_K^{n+1} - u_K^n) \quad (11)$$

$$+ \frac{\delta t}{|A_K|} \sum_{T \in T_K} \sum_{L \in \mathcal{V}_T \setminus \{K\}} \eta_{KL}^{n+1} \Lambda_{KL}^T (u_K^{n+1} - u_L^{n+1}) = \delta t f_K^{n+1}, \quad \forall K \in \mathcal{V} \setminus \mathcal{V}^D$$

$$u_K^{n+1} = 0 \quad \forall K \in \mathcal{V}^D. \quad (12)$$

Remark 2. We would like to stress that our approach remains valid for any scheme that can be recast under the two-point like formulation (11). For instance, this is the case of the combined finite volume–nonconforming/mixed-hybrid finite element method proposed in [23]. A similar extension can be performed to the DDFV schemes following the spirit of the work [41].

4.2 The weakly monotonicity of the scheme

Let us now prove a central property of the proposed numerical scheme.

Proposition 3. *The nonlinear finite volume scheme (11) is weakly monotone in the sense that*

$$u_K^n \geq g_K, \quad \forall n \in [0, n_f], \quad \forall K \in \mathcal{V}.$$

Proof. The property is shown by induction on n . Thanks to the hypothesis (\mathbf{H}_1) , it is true for $n = 0$. Now, assume that the claim is true up to the time step $n < n_f$ i.e., $u_K^n \geq g_K$. Select a control volume A_K such that $u_K^{n+1} = \min_{L \in \mathcal{V} \setminus \mathcal{V}^D} u_L^{n+1}$. Next, the goal is to establish that we still have $u_K^{n+1} \geq g_K$, $\forall K \in \mathcal{V} \setminus \mathcal{V}^D$ by contradiction. For this purpose, assume that $u_K^{n+1} < g_K$. Then, multiply the equation of (11), corresponding to the underlined K , by $(u_K^{n+1} - g_K)$ to obtain

$$\begin{aligned} & \phi_K(u_K^{n+1} - u_K^n)(u_K^{n+1} - g_K) \\ & + \frac{\delta t}{|A_K|} \sum_{T \in T_K} \sum_{L \in \mathcal{V}_T \setminus \{K\}} \eta_{KL}^{n+1} \Lambda_{KL}^T (u_K^{n+1} - u_L^{n+1})(u_K^{n+1} - g_K) = \delta t f_K (u_K^{n+1} - g_K). \end{aligned} \quad (13)$$

Splitting $\Lambda_{KL}^T = (\Lambda_{KL}^T)^+ - (\Lambda_{KL}^T)^- = \max(\Lambda_{KL}^T, 0) - \max(-\Lambda_{KL}^T, 0)$ entails

$$\begin{aligned} & \phi_K(u_K^{n+1} - u_K^n)(u_K^{n+1} - g_K) \\ & + \frac{\delta t}{|A_K|} \sum_{T \in T_K} \sum_{L \in \mathcal{V}_T \setminus \{K\}} \eta_{KL}^{n+1} (\Lambda_{KL}^T)^+ (u_K^{n+1} - u_L^{n+1})(u_K^{n+1} - g_K) \\ & - \frac{\delta t}{|A_K|} \sum_{T \in T_K} \sum_{L \in \mathcal{V}_T \setminus \{K\}} \eta_{KL}^{n+1} (\Lambda_{KL}^T)^- (u_K^{n+1} - u_L^{n+1})(u_K^{n+1} - g_K) = \delta t f_K (u_K^{n+1} - g_K). \end{aligned}$$

One checks that $\phi_K(u_K^{n+1} - u_K^n)(u_K^{n+1} - g_K) = \phi_K(u_K^{n+1} - g_K + g_K - u_K^n)(u_K^{n+1} - g_K) > 0$. Bearing in mind $u_K^{n+1} \leq u_L^{n+1}$, one deduces that

$$\frac{\delta t}{|A_K|} \sum_{T \in T_K} \sum_{L \in \mathcal{V}_T \setminus \{K\}} \eta_{KL}^{n+1} (\Lambda_{KL}^T)^+ (u_K^{n+1} - u_L^{n+1})(u_K^{n+1} - g_K) \geq 0.$$

In the case where the negative transmissibility is active, the coefficient η_{KL}^{n+1} is forced to vanish by construction because $u_K^{n+1} < g_K$. As a consequence, there holds

$$-\frac{\delta t}{|A_K|} \sum_{T \in \mathcal{T}_K} \sum_{L \in \mathcal{V}_T \setminus \{K\}} \eta_{KL}^{n+1} (\Lambda_{KL}^T)^- (u_K^{n+1} - u_L^{n+1}) (u_K^{n+1} - g_K)^- = 0.$$

The right hand side in (13) is nonpositive. The equation (13) only holds true if $(u_K^{n+1} - g_K) = 0$, which is absurd. Consequently, we find that

$$u_L^{n+1} \geq u_K^{n+1} \geq g_K \quad \forall n = 0, \dots, n_f - 1, \quad \forall L \in \mathcal{V} \setminus \mathcal{V}^D.$$

This ends the proof. \square

Remark 3. Recall that a scheme is said to be monotone if $u_0 \geq g$ implies $u_T \geq g$ independently of the discretization. This is not the case of our approach because the underlined property depends on the scheme. The function g is present in the corrected flux. Then, if g changes the latter also changes. For this reason we called it a weakly monotone finite volume scheme.

Remark 4. As we already mentioned, the current weakly monotone scheme exhibits a stronger property in terms of the discrete maximum principle. Indeed, in the works [41, 37, 38, 11, 39] the obtained numerical solution is either positive or nonnegative. This can be also reached by setting $g = 0$ in our scheme.

4.3 A priori estimates

This subsection is devoted to the proof of the a priori estimates. Before that, we will make use of the following result. It provides equivalence between some discrete norms, which is fundamental to derive the appropriate estimations on the system's energy and on the gradient of the Kirchhoff's transform. The proof can be consulted in [7, 11]. Another formulation was highlighted in [27].

Lemma 4. There exists a constant C that depends only on $\theta_{\mathcal{T}}$, $\underline{\Lambda}$ and $\bar{\Lambda}$ such that for any $s_{\mathcal{T}} \in \mathcal{H}_{\mathcal{T}}$

$$\sum_{T \in \mathcal{T}} \sum_{\sigma_{KL}^T \in \mathcal{E}_T^*} |\Lambda_{KL}^T| (s_K - s_L)^2 \leq C \sum_{T \in \mathcal{T}} \sum_{\sigma_{KL}^T \in \mathcal{E}_T^*} \Lambda_{KL}^T (s_K - s_L)^2 = C \int_{\Omega} \Lambda \nabla s_{\mathcal{T}} \cdot \nabla s_{\mathcal{T}} dx. \quad (14)$$

To ease the readability of the scheme analysis, we use the following abbreviated notation

$$\xi_K^{n+1} = \xi(u_K^{n+1}), \quad \forall K \in \mathcal{V}, \quad \forall n \in \{0, \dots, n_f - 1\}.$$

Let us set

$$\tilde{\eta}_{KL}^{n+1} = \begin{cases} \left(\frac{\xi_K^{n+1} - \xi_L^{n+1}}{u_K^{n+1} - u_L^{n+1}} \right)^2 & \text{if } u_K^{n+1} \neq u_L^{n+1}, \\ \eta(u_K^{n+1}) & \text{if } u_K^{n+1} = u_L^{n+1}. \end{cases}$$

The importance of this formula resides in the fact that

$$\tilde{\eta}_{KL}^{n+1} \left(u_K^{n+1} - u_L^{n+1} \right)^2 = \left(\xi_K^{n+1} - \xi_L^{n+1} \right)^2. \quad (15)$$

Additionally, one has $\eta_T^{n+1} \geq \tilde{\eta}_{KL}^{n+1}/3$. Indeed, from the continuity of η , one obtains

$$\tilde{\eta}_{KL}^{n+1} = \eta(\hat{u}_{KL}^{n+1})$$

for some \hat{u}_{KL}^{n+1} in the ranges of u_K^{n+1} and u_L^{n+1} . On the other hand, observe that

$$\eta_T^{n+1} \geq \frac{1}{3} \max_{a \in I_{KL}^{n+1}} \eta(a) \geq \tilde{\eta}_{KL}^{n+1}/3, \quad (16)$$

where $I_{KL}^{n+1} = [\min(u_K^{n+1}, u_L^{n+1}), \max(u_K^{n+1}, u_L^{n+1})]$.

Proposition 5. *There exists a positive constant C depending only on the physical data and θ_T such that the following energy estimates hold true*

$$\sum_{n=0}^{n_f-1} \delta t \|\nabla \xi_{\mathcal{T}}^{n+1}\|_{L^2(\Omega)}^2 \leq C, \quad (17)$$

$$\sum_{n=0}^{n_f-1} \delta t \sum_{T \in \mathcal{T}} \sum_{\sigma_{KL}^T \in \mathcal{E}_T^+} |\Lambda_{KL}^T| \eta_{KL}^{n+1} (u_K^{n+1} - u_L^{n+1})^2 \leq C. \quad (18)$$

Proof. We prove the first estimation. Multiply the scheme (11) by $|A_K|u_K^{n+1}$, and we sum on all $K \in \mathcal{V} \setminus \mathcal{V}^D$ and all $n \in \{0, \dots, n_f - 1\}$, the result is written as

$$S_1 + S_2 = S_2.$$

where

$$\begin{aligned} S_1 &= \sum_{n=0}^{n_f-1} \sum_{K \in \mathcal{V} \setminus \mathcal{V}^D} |A_K| \phi_K(u_K^{n+1} - u_K^n) u_K^{n+1}, \\ S_2 &= \sum_{n=0}^{n_f-1} \delta t \sum_{K \in \mathcal{V} \setminus \mathcal{V}^D} \sum_{T \in \mathcal{T}_K} \sum_{L \in \mathcal{V}_T \setminus \{K\}} \eta_{KL}^{n+1} \Lambda_{KL}^T (u_K^{n+1} - u_L^{n+1}) u_K^{n+1}, \\ S_3 &= \sum_{n=0}^{n_f-1} \delta t \sum_{K \in \mathcal{V} \setminus \mathcal{V}^D} |A_K| f_K^{n+1} u_K^{n+1}. \end{aligned}$$

Apply the convexity inequality $(a - b)b \geq \frac{1}{2}(a^2 - b^2)$, $\forall a, b \in \mathbb{R}$, to deduce that S_1 is greater than a telescopic series yielding

$$\begin{aligned}
S_1 &\geq \frac{1}{2} \sum_{n=0}^{n_f-1} \sum_{K \in \mathcal{V} \setminus \mathcal{V}^D} |A_K| \phi_K \left((u_K^{n+1})^2 - (u_K^n)^2 \right) \\
&\geq \frac{1}{2} \sum_{K \in \mathcal{V}} |A_K| \phi_K (u_K^{n_f})^2 - \frac{1}{2} \sum_{K \in \mathcal{V}} |A_K| \phi_K (u_K^0)^2.
\end{aligned}$$

Next, rearranging the terms of S_2 by triangles and dual edges of these triangles leads to

$$S_2 = \sum_{n=0}^{n_f-1} \delta t \sum_{T \in \mathcal{T}} \sum_{\sigma_{KL}^T \in \mathcal{E}_T^*} \eta_{KL}^{n+1} \Lambda_{KL}^T (u_K^{n+1} - u_L^{n+1})^2.$$

Thanks to the crucial definition of η_{KL}^{n+1} given in (8), one infers

$$\eta_{KL}^{n+1} = \eta_T^{n+1}, \quad \forall \Lambda_{KL}^T \geq 0 \quad \text{and} \quad \eta_{KL}^{n+1} \leq \eta_T^{n+1}, \quad \forall \Lambda_{KL}^T < 0. \quad (19)$$

As a consequence of this and Lemma 4 we obtain

$$\begin{aligned}
S_2 &\geq \sum_{n=0}^{n_f-1} \delta t \sum_{T \in \mathcal{T}} \eta_T^{n+1} \sum_{\sigma_{KL}^T \in \mathcal{E}_T^*} \Lambda_{KL}^T (u_K^{n+1} - u_L^{n+1})^2, \\
&\geq \underbrace{\frac{1}{C_0} \sum_{n=0}^{n_f-1} \delta t \sum_{T \in \mathcal{T}} \eta_T^{n+1} \sum_{\sigma_{KL}^T \in \mathcal{E}_T^*} |\Lambda_{KL}^T| (u_K^{n+1} - u_L^{n+1})^2}_{2 \times \widehat{S}_2}.
\end{aligned}$$

Now, combine (15), (16) and the ellipticity of the tensor Λ to find

$$\begin{aligned}
\widehat{S}_2 &\geq \frac{1}{6C_0} \sum_{n=0}^{n_f-1} \delta t \sum_{T \in \mathcal{T}} \sum_{\sigma_{KL}^T \in \mathcal{E}_T^*} \Lambda_{KL}^T \left(\xi_K^{n+1} - \xi_L^{n+1} \right)^2 \\
&\geq C'_1 \sum_{n=0}^{n_f-1} \delta t \|\nabla \xi_{\mathcal{T}}^{n+1}\|_{L^2(\Omega)}^2, \quad C'_1 = \frac{\Lambda}{6C_0}.
\end{aligned}$$

Using the Cauchy-Schwarz inequality, Young's inequality and Assumptions **(H₃)**, **(H₆)**, it can be checked that

$$S_3 \leq C'_2 \|f\|_{L^2(Q_{t_f})}^2 + \frac{C'_1}{2} \sum_{n=0}^{n_f-1} \delta t \|\nabla \xi_{\mathcal{T}}^{n+1}\|_{L^2(\Omega)}^2,$$

for some constant $C'_2 > 0$ independent of $h_{\mathcal{T}}$ and δt . Gathering the estimations of S_1 , S_2 and S_3 we finally prove that

$$\sum_{n=0}^{n_f-1} \delta t \|\nabla \xi_{\mathcal{T}}^{n+1}\|_{L^2(\Omega)}^2 + \sum_{n=0}^{n_f-1} \delta t \sum_{T \in \mathcal{T}} \eta_T^{n+1} \sum_{\sigma_{KL}^T \in \mathcal{E}_T^*} |\Lambda_{KL}^T| (u_K^{n+1} - u_L^{n+1})^2 \leq C'_3.$$

As a consequence, we deduce

$$\begin{aligned}
0 &\leq \sum_{n=0}^{n_f-1} \delta t \sum_{T \in \mathcal{T}} \sum_{\sigma_{KL}^T \in \mathcal{E}_T^*} \Lambda_{KL}^T \eta_{KL}^{n+1} (u_K^{n+1} - u_L^{n+1})^2 \\
&\leq \sum_{n=0}^{n_f-1} \delta t \sum_{T \in \mathcal{T}} \eta_T^{n+1} \sum_{\sigma_{KL}^T \in \mathcal{E}_T^*} |\Lambda_{KL}^T| (u_K^{n+1} - u_L^{n+1})^2 \\
&\leq \sum_{n=0}^{n_f-1} \delta t \sum_{T \in \mathcal{T}} \eta_T^{n+1} \sum_{\sigma_{KL}^T \in \mathcal{E}_T^*} |\Lambda_{KL}^T| (u_K^{n+1} - u_L^{n+1})^2 \leq C'_3.
\end{aligned}$$

Hence, the proof of Proposition 5 is complete. \square

4.4 Existence of discrete solution

The existence result is shown via the following consequence of the fixed point theorem [18].

Lemma 6. *Let \mathcal{X} be a finite dimensional space equipped with the inner product denoted by $\langle \cdot, \cdot \rangle_{\mathcal{A}}$. Let \mathcal{P} be a continuous mapping from \mathcal{A} into \mathcal{A} satisfying the monotony criterion:*

$$\text{there exists } r > 0 \text{ such that } \langle \mathcal{P}(z), z \rangle_{\mathcal{A}} > 0 \text{ for all } z \in \mathcal{A} \text{ with } \|z\|_{\mathcal{X}} = r.$$

Then, there exists $z_0 \in \mathcal{A}$ with $\|z_0\|_{\mathcal{X}} = r$ such that $\mathcal{P}(z_0) = 0$.

Proposition 7. *There exists a solution $(u_K^{n+1})_{K \in \mathcal{V}, n=0, \dots, n_f-1}$ to the weakly monotone finite volume scheme (11)-(12). It further satisfies the physical range claimed in Proposition 3.*

Proof. The proof is proceeded on the time level n by induction. First, let us set the following notations

$$\mathcal{N} = \text{card}(\mathcal{V} \setminus \mathcal{V}^D), \quad u_{\mathcal{V}} = \{u_K^{n+1}\}_{K \in \mathcal{V} \setminus \mathcal{V}^D} \in \mathbb{R}^{\mathcal{N}}.$$

In the sequel, the implicit character in time is omitted to ease the readability. We define the nonlinear mapping

$$\begin{aligned}
\mathcal{P} &: \mathbb{R}^{\mathcal{N}} \longrightarrow \mathbb{R}^{\mathcal{N}} \\
u_{\mathcal{V}} &\longrightarrow \mathcal{P}(u_{\mathcal{V}})
\end{aligned}$$

where the components of $\mathcal{P}(u_{\mathcal{V}})$ write

$$\mathcal{P}(u_{\mathcal{V}})|_K = \phi_K(u_K - u_K^n) + \frac{\delta t}{|A_K|} \sum_{T \in \mathcal{T}_K} \sum_{L \in \mathcal{V}_T \setminus \{K\}} \Lambda_{KL}^T \eta_{KL} (u_K - u_L) - \delta t f_K.$$

Then a root of \mathcal{P} i.e., $\mathcal{P}(u_{\mathcal{V}}) = 0$ is necessary a solution to the finite volume scheme. Here, the objective is to prove that $\mathcal{P}(u_{\mathcal{V}}) \cdot u_{\mathcal{V}} > 0$ for $\|u_{\mathcal{V}}\|_{\mathbb{R}^{\mathcal{N}}} = r$

where the radius r is sufficiently large. Being inspired by the proof of Proposition 5 we compute

$$\begin{aligned} \mathcal{P}(u_{\mathcal{V}}) \cdot u_{\mathcal{V}} &\geq -\frac{1}{2\delta t} \sum_{K \in \mathcal{V} \setminus \mathcal{V}^D} |A_K| \phi_K (u_K^n)^2 + \frac{\phi_0}{2\delta t} \sum_{K \in \mathcal{V} \setminus \mathcal{V}^D} |A_K| (u_K)^2 \\ &\quad + C' \|\nabla \xi_{\mathcal{T}}\|_{L^2(\Omega)}^2 - C'' \geq -\frac{1}{2\delta t} \|u_{\mathcal{T}}^n\|_{L^2(\Omega)}^2 + \frac{\phi_0}{2\delta t} \|u_{\mathcal{T}}\|_{L^2(\Omega)}^2 - C''. \end{aligned}$$

Introducing the equivalence of norms in $\mathbb{R}^{\mathcal{N}}$ and taking $\|u_{\mathcal{T}}\|_{L^2(\Omega)}^2$ sufficiently large, we end up with $\mathcal{P}(u_{\mathcal{V}}) \cdot u_{\mathcal{V}} > 0$. Thus, Lemma 6 ensures the existence of at least one solution to the numerical scheme (11)-(12). The obtained solution obeys naturally the physical range claimed in Proposition 3. This concludes the proof of Proposition 7. \square

5 Numerical results

In this section, we first conduct a battery of numerical tests to validate the proposed weakly monotone finite volume approach. In a second stage, we will apply the method for the simulation of mass diffusion in hygroscopic media of wood type.

5.1 Accuracy and stability assessment

We look at and evaluate the scheme's behavior in terms of accuracy and the discrete maximum principle. In other words, the resulting algorithm is examined to scrutinize the validity of the following elements simultaneously for which the scheme is constructed.

- Ensure the second order accuracy (when the solution is smooth enough).
- Honor the prescribed maximum principle i.e., $u^0 \geq g \implies u_{\mathcal{T}}^{n+1} \geq g$.

The numerical scheme gives rise to a discrete nonlinear system that is solved owing to the Newton-Raphson method at each time level. The tolerance is fixed to $\epsilon = 10^{-12}$. The convergence criterion is made on the successive iterates of the algorithm. We would like to underline that the weakly monotone property is not necessarily satisfied at the early iterations of the nonlinear solver in general, it is only achieved at the convergence stage. The implementation was carried out in Matlab.

In all the tests of this subsection, the final time is set to $t_f = 0.2$. The porosity function is given by $\phi = 1$ and there is no source term i.e., $f = 0$. The computational domain is the unit square $\bar{\Omega} = [0, 1]^2$, it is meshed by 4 successively refined meshes taken from the FVCA5 benchmark [29] on diffusion problems. An illustration of the first meshes is given in Figure 2. The time step is proportional to the square of the mesh size so that one can avoid the impact of the time discretization, which is of first order.

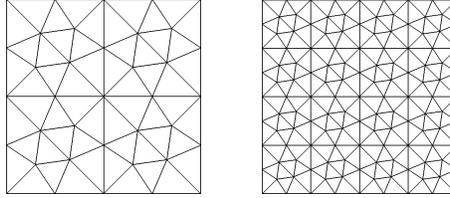


Figure 2: First and second triangular meshes of the FVCA5 benchmark. Their number of vertices (triangles) are 37 (56) and 129 (224) respectively.

The accuracy is judged by computing the errors between the piecewise constant numerical solution $u_{\mathcal{T},\delta t}$ against the manufactured exact solution u_{ext} . The latter is taken at the mesh vertices. Then, we consider

$$\text{err}_{L^p} = \|u_{\mathcal{T},\delta t} - u_{ext}\|_{L^p(Q_{t_f})} \quad p = 1, 2, \infty.$$

The convergence order is measured using the formula

$$\text{Rate} = \frac{\log(\text{err}_{L^p}^{i+1}/\text{err}_{L^p}^i)}{\log(h^{i+1}/h^i)},$$

where $i = 1, \dots, 4$ denotes the triangulation label. The diffusion tensor and the nonlinearities are peculiar to each test.

5.1.1 Accuracy test

The aim of this preliminary test is to select an appropriate value of the parameter $\gamma_{\mathcal{T}}$. In this case, the model problem is the anisotropic heat equation supplemented by the homogeneous Neumann condition on the full boundary

$$u_t - \text{div}(\Lambda \nabla u) = 0,$$

where the diffusion tensor Λ is diagonal

$$\Lambda = \begin{pmatrix} a_x & 0 \\ 0 & a_y \end{pmatrix}.$$

It is taken highly anisotropic with $a_x = 1$ and $a_y = 1000$. The function g is fixed to 0. An exact solution to the above problem is manufactured under as

$$u(x, y, t) = \frac{1}{2} \left(1 + \cos(\pi x) \exp(-a_x \pi^2 t) \right), \quad \forall (x, y, t) \in \Omega \times [0, t_f].$$

There is no systematic good selection of the parameter $\gamma_{\mathcal{T}}$ appearing in the expression (9). Therefore, we perform three choices to justify numerically the adequate one. For this purpose, we evaluate the error err_{L^2} and show how the numerical solution behaves according to each $\gamma_{\mathcal{T}}$. First, four static decreasing values are given i.e., $\gamma_{\mathcal{T}} \in \{0.1, 0.01, 0.001, 0.0001\}$. The results are given in

the left of Figure 3. A deterioration of the accuracy is observed as the mesh is refined. To correct this issue, we consider a parameter that is depending on the mesh size as follows $\gamma_{\mathcal{T}} \in \{h, 0.1h, 0.05h, 0.01h\}$. The corresponding results shown in medium of Figure 3 exhibit poor convergence rates. This has led to propose $\gamma_{\mathcal{T}} \in \{h^2, 0.1h^2, 0.05h^2, 0.01h^2\}$. Thereby, one recovers the second order accuracy.

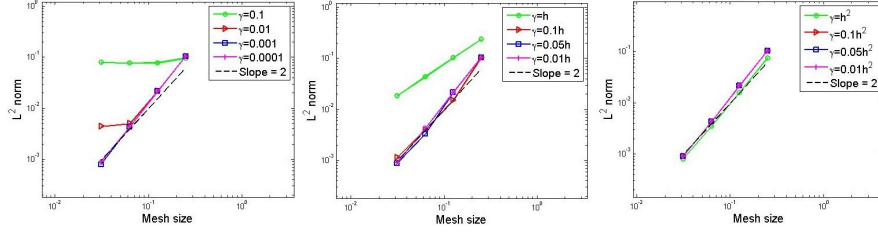


Figure 3: Test 1: the L^2 errors according to the chosen $\gamma_{\mathcal{T}}$.

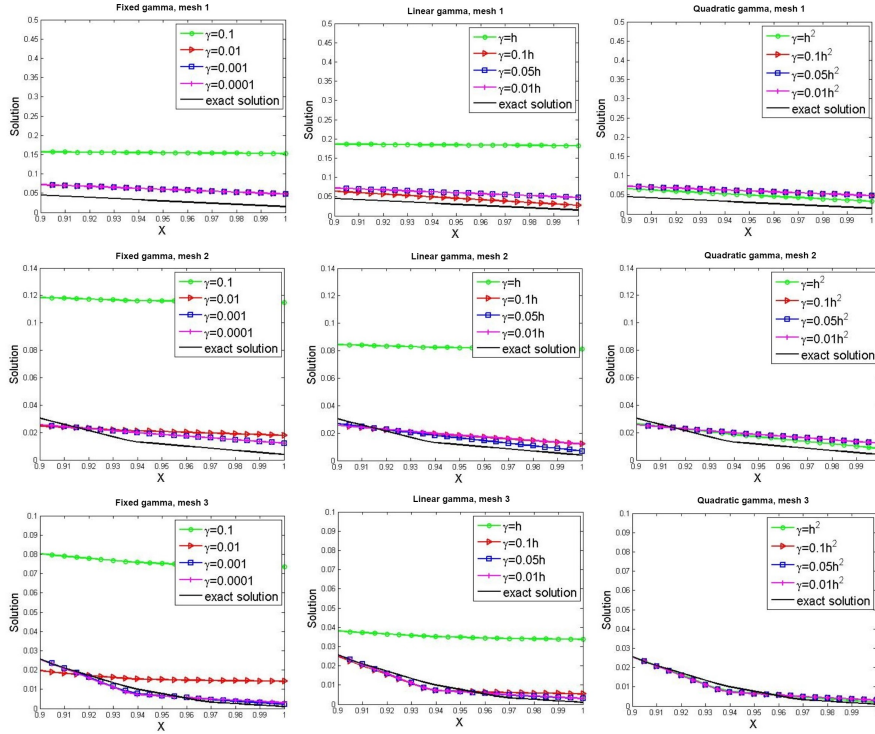


Figure 4: Test 1: magnification on the cross section of the solution at the point 0 in terms of $\gamma_{\mathcal{T}}$ and the mesh.

In Figure 4, the numerical solution is shown along the line $\{y = 0\}$ and the magnification of the plotted values are between 0.1 and 0.9. In rows, the mesh is fixed and $\gamma_{\mathcal{T}}$ varies. In columns, the mesh size is decreasing whereas $\gamma_{\mathcal{T}}$ is taken by category. The figures of fixed $\gamma_{\mathcal{T}}$ present inaccurate results, especially when the mesh is refined. If $\gamma_{\mathcal{T}}$ is linear with respect to h , the accuracy is improved, but the method still suffers from excessive numerical diffusion. The last case where $\gamma_{\mathcal{T}} \sim h^2$ corrects this inconvenience and offers a good convergence towards the exact solution.

Accordingly, this quadratic proportionality with respect to the mesh size yields satisfactory behavior of the accuracy and the solution profile. It was also checked that the numerical solution honors the positivity at each case. Consequently, in the rest of the paper, we fix $\gamma_{\mathcal{T}} = h^2$.

5.1.2 Positivity test

The objective here is to compare efficiency of the linear CVFE scheme with our novel weakly nonlinear monotone finite volume (WMFV) for the heat equation (HE). We consider the same problem as in the previous example. In this test-case, the function g is fixed to zero. Then, the numerical solution of the WMFV method is expected to be nonnegative.

The behavior of the schemes is indicated in Tables 1–2. We retain that the convergence rate for both methods reaches the order two. The WMFV approach exhibits a larger error magnitude. Besides, the linear CVFE scheme suffers from undershoots spanned by the anisotropy. However, the nonlinear WMFV scheme preserves the positivity of the solution. Finally, there is no significant difference in terms of the computational cost measured by the number of the Newton-solver iterations.

h	err_{L^1}	rate	err_{L^2}	rate	err_{L^∞}	rate	u_{\min}	Newton
0.250	0.0412	-	0.0465	-	0.0691	-	-0.0392	62
0.125	0.0100	2.0441	0.0115	2.0120	0.0204	1.7568	-0.0123	256
0.063	0.0025	2.0338	0.0029	2.0278	0.0053	1.9587	-0.0032	1006
0.0310	6.20E-04	1.9543	7.19E-04	1.9527	0.0014	1.9315	-0.0008	4162

Table 1: Test 2 : accuracy results of the CVFE scheme for the HE with $a_x = 1$ and $a_y = 1000$

h	err_{L^1}	rate	err_{L^2}	rate	err_{L^∞}	rate	u_{\min}	Newton
0.250	0.1061	-	0.1137	-	0.1690	-	0.1837	118
0.125	0.0165	2.6839	0.0222	2.3593	0.0475	1.8309	0.0460	302
0.063	0.0031	2.4343	0.0045	2.3382	0.0134	1.8518	0.0117	1048
0.0310	6.91E-04	2.1210	9.29E-04	2.21	0.0034	1.9353	0.0028	4203

Table 2: Test 2 : accuracy results of the WMFV scheme for the HE with $a_x = 1$ and $a_y = 1000$.

5.1.3 Nonlinear diffusion test

In this test-case, we are always interested in the heat equation. The goal is to compare the monotonicity behavior of the linear CVFE and the nonlinear WMFV schemes in the presence of a tough initial condition and a highly anisotropic tensor.

The initial solution is chosen as

$$u_0(x, y) = \begin{cases} -\frac{(1-0.2)}{0.3}x + 1 & \text{if } 0 \leq x \leq 0.2, \\ \frac{1}{0.2-0.5}(x - 0.5) & \text{if } 0.2 < x \leq 0.5, \\ 0 & \text{if } 0.5 < x \leq 1. \end{cases} \quad (20)$$

The boundary is divided into two parts $\partial\Omega = \partial\Omega^D \cup \partial\Omega^N$.

- On $\partial\Omega^D = \{x = 0\} \cup \{x = 1\}$ Dirichlet's condition agrees with the initial solution (20).
- On $\partial\Omega^N = \{y = 0\} \cup \{y = 1\}$ homogeneous Neumann's boundary condition is maintained.

The anisotropy matrix is given by

$$\Lambda = \frac{1}{x^2 + y^2} \begin{pmatrix} \delta x^2 + y^2 & (1 - \delta)xy \\ (1 - \delta)xy & x^2 + \delta y^2 \end{pmatrix},$$

where δ accounts for the anisotropy ratio that is fixed to 10^{-3} . It is approximated at the center of the triangles. The function g is fixed to u_0 .

Using these data, we run the linear CVFE algorithm and the WMFV one. The first three iterations in time on the third mesh are considered. The 2D view of the solution is given in Figure 5. The dots refer to the position of undershoots. For comparison, we plot in Figure 6 the solution profiles along the line $\{y = 1\}$. As a result, the upper figures show that the CVFE solution goes down the function $g = u^0$ and suffers from undershoots, which is classical for linear methods. Nevertheless, the solution obtained by the nonlinear WMFV scheme remains bigger than the initial condition. Then, the weakly monotone scheme can preserve piecewise linear bounds. This feature cannot be captured by the schemes developed in [41, 37, 39, 11, 28] because the solutions obtained by these works are only preserving the positivity. Consequently, positive or in general minimum-preserving schemes are not necessarily satisfying the weakly monotone property.

5.1.4 Porous medium equation (PME) test (anisotropy case)

In this test-case, we focus on a nonlinear degenerate problem of the anisotropic porous medium equation type

$$u_t - \operatorname{div}(2|u|\Lambda\nabla u) = 0.$$

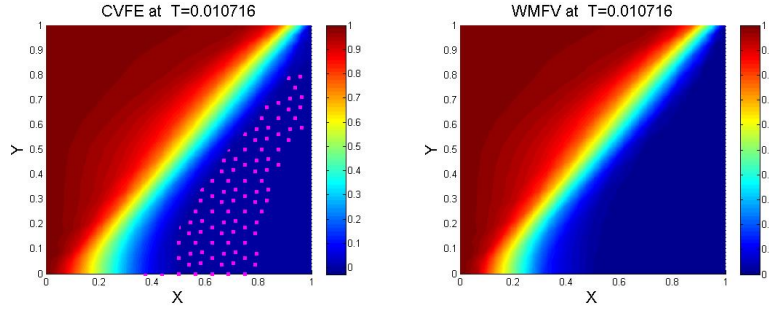


Figure 5: Test 3 : CVFE solution (left) and WMFV solution (right) at the third iteration in time on the third mesh. The magenta dots refer to the presence of undershoots.

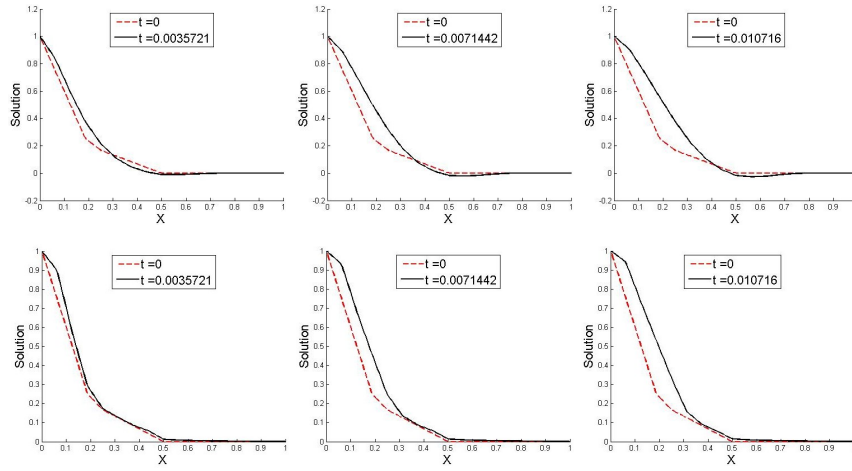


Figure 6: Test 3 : 1D cross section of the solutions produced by the linear CVFE scheme (top) and the nonlinear WMFV scheme (bottom) for the first three iterations in time on the third mesh.

As in Test 1, the diffusion tensor is diagonal and anisotropic such that $a_x = 1$ and $a_y = 100$. A fully nonhomogeneous Dirichlet boundary condition is considered here. It agrees with the one-dimensional analytical solution

$$u(x, y, t) = \max(2a_x t - x, 0), \quad \forall (x, y) \in \Omega, \quad \forall t \in (0, t_f).$$

The obtained accuracy results are presented in Tables 3–4. Because the solution is not smooth enough, the accuracy is less than the second order. The quasilinear scheme yields to undershoots but produces smaller errors. On the other hand, the WMFV methodology is positive and gives rise to relatively bigger errors. More importantly, improved convergence rates are noticed for the WMFV scheme contrary to the CVFE version. The behavior of the Newton solver is similar.

h	err $_{L^1}$	rate	err $_{L^2}$	rate	err $_{L^\infty}$	rate	u_{\min}	Newton
0.250	0.0086	-	0.0187	-	0.0602	-	-5.10e-04	128
0.125	0.0029	1.5442	0.0070	1.4226	0.0308	0.9684	-3.66e-05	512
0.063	0.0010	1.5659	0.0029	1.2602	0.0158	0.9713	-2.47e-06	1830
0.0310	2.90E-04	1.7448	0.0012	1.2805	0.0088	0.8285	-1.41e-07	6261

Table 3: Test 4 : accuracy results for the quasilinear scheme with $a_x = 1$ and $a_y = 100$.

h	err $_{L^1}$	rate	err $_{L^2}$	rate	err $_{L^\infty}$	rate	u_{\min}	Newton
0.250	0.0228	-	0.0360	-	0.0985	-	0	127
0.125	0.0082	1.4729	0.0137	1.3988	0.0480	1.0379	0	511
0.063	0.0017	2.2825	0.0042	1.7313	0.0214	1.1782	0	1825
0.0310	3.00E-04	2.4597	0.0012	1.7585	0.0103	1.0315	0	6242

Table 4: Test 4 : accuracy results for the nonlinear MFV scheme with $a_x = 1$ and $a_y = 100$.

5.1.5 PME test (heterogeneous rotating anisotropy case)

This last example problem aims to test the capability of the WMVF method in preserving the property of weak monotonicity. A particular emphasis is set on the non-degeneracy of the solution. The model is the anisotropic porous medium equation

$$u_t - \operatorname{div}(\Lambda \nabla u^2) = 0.$$

We apply a heterogeneous rotating anisotropic tensor

$$\Lambda = \begin{pmatrix} \cos(\pi x) & -\sin(\pi x) \\ \sin(\pi x) & \cos(\pi x) \end{pmatrix} \begin{pmatrix} 0.1 & 0 \\ 0 & 100 \end{pmatrix} \begin{pmatrix} \cos(\pi x) & \sin(\pi x) \\ -\sin(\pi x) & \cos(\pi x) \end{pmatrix}.$$

We choose the condition initial as follows

$$u(x, y, 0) = \begin{cases} -\frac{(1-0.2)}{0.3}x + 1 & \text{if } 0 \leq x \leq 0.3, \\ 0.2 & \text{if } 0.3 < x \leq 0.7, \\ \frac{(1-0.2)}{(1-0.7)}(x - 0.7) + 0.2 & \text{if } 0.7 < x \leq 1. \end{cases} \quad (21)$$

The function g is fixed to u_0 . Similarly to Test 3, the boundary is divided into two parts.

- On $\partial\Omega^D = \{x = 0\} \cup \{x = 1\}$ Dirichlet's condition is taken according to the initial solution (21).
- On $\partial\Omega^N = \{y = 0\} \cup \{y = 1\}$ one considers the homogeneous Neumann condition.

The outcomes of this test are shown in Figure 7, in the case of three iterations in time, namely 2, 4 and 10 iterations. The first row corresponds to the results of the CVFE scheme while the second row indicates the results of the proposed

WMFV approach. This example highlights the failure of the standard CVFE scheme in capturing the expected behavior of the numerical solution, where it spreads out of the limited function g . This can be also observed on the 2D view of the solution exhibited in Figure 8. In the left side, the plotted dots stand for undershoots. The WMFV solution behaves naturally where it remains inside the convex hull delimited by g , which confirms the robustness of the novel scheme in reinforcing the monotonicity property despite the toughness of the input data.

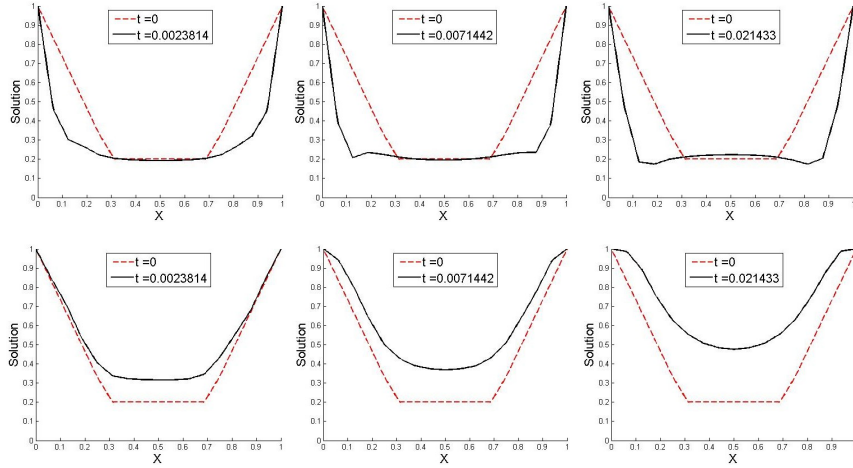


Figure 7: Test 5 : results of the linear CVFE scheme (top) and the nonlinear MFV scheme (bottom) for the iterations 2, 4 et 10 in time and on the third mesh.

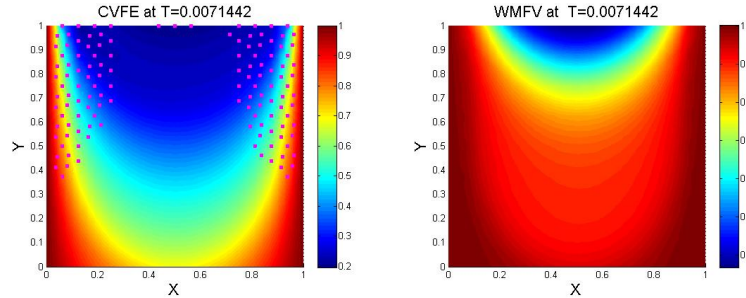


Figure 8: Test 5 : solution of the linear CVFE scheme (left) and nonlinear WMFV scheme (right) for the iteration 3 in time and on the third mesh. The magenta dots refer to the presence of undershoots.

5.2 Mass diffusion in hygroscopic media of the wood type

In this last section, we propose application examples of the new scheme proposed in the present work. Water diffusion in wood, a strongly anisotropic medium, is chosen as severe test. Also a comparison with the standard CVFE scheme is provided. In the sequel, dimensionless quantities are taken into account and they are understood in the macroscopic level. We consider the wood species of type poplar. The considered model is purely diffusive

$$\phi u_t - \operatorname{div}(\Lambda \nabla \varphi(u)) = 0.$$

5.3 Test A

In a first moment we look at the case where $\varphi(u) = u$. The domain occupied by the sample is the unit square. It is first meshed using the third triangulation the FVCA5 benchmark [29]. Then, the vertices are amended using the perturbation

$$x_{\text{new}} = x_{\text{old}} + \alpha R_x h_{\mathcal{T}}, \quad y_{\text{new}} = y_{\text{old}} + \alpha R_y h_{\mathcal{T}},$$

where R_x, R_y are random numbers between $[-0.5, 0.5]$ and $\alpha = 0.25$ is the distortion factor. In all the tests below, the time step is $\delta t = 0.5h_{\mathcal{T}}^2$. The boundary is divided into three parts $\partial\Omega = \partial\Omega_{(1)}^D \cup \partial\Omega_{(2)}^D \cup \partial\Omega^N$ where

$$\partial\Omega_{(1)}^D = [0.4, 0.6] \times \{y = 0\}, \quad \partial\Omega_{(2)}^D = [0, 1] \times \{y = 1\}, \quad \partial\Omega^N = \partial\Omega \setminus (\partial\Omega_{(1)}^D \cup \partial\Omega_{(2)}^D).$$

An illustration of the used mesh is plotted in the left side of Figure 9. Next, a discontinuous boundary condition is taken $\partial\Omega_{(1)}^D$ i.e., it is equal to 0.9 in $[0, t_f/2]$ and it switches to 0.3 in $(t_f/2, t_f]$. The free-flow condition is imposed on $\partial\Omega_{(2)}^D$.

Following [40], the porosity of the poplar sample is fixed to $\phi = 0.62$. We assume that the anisotropy of the cell walls is modeled by

$$\Lambda(x, y) = \begin{pmatrix} \cos(\theta) & \sin(\theta) \\ -\sin(\theta) & \cos(\theta) \end{pmatrix} \begin{pmatrix} 0.2x & 0 \\ 0 & 0.6 \exp(-1.5y) \end{pmatrix} \begin{pmatrix} \cos(\theta) & -\sin(\theta) \\ \sin(\theta) & \cos(\theta) \end{pmatrix}, \quad \forall (x, y) \in \Omega.$$

The angle θ is assigned to $\pi/6$. The vector field generated by this matrix is shown in the right side of Figure 9.

We performed three tests according to the final times $t_f = 0.03, 0.2, 1$. The outcomes of this simulation are displayed in Figure 10. The upper row corresponds to the CVFE solutions while the lower row shows the results of the WMFV methodology. In both situations, the numerical solutions are quite similar and they follow the preferential directions prescribed by the tensor Λ . This anisotropy leads to several undershoots represented by the magenta dots in the linear case. On the other hand, the WMFV solutions are free of such oscillations.

5.4 Test B

In a second time, we are concerned with the case where $\varphi(u) = -\log(1-u)$. Such a function accounts for the behavior of the capillary pressure. Now, the sample

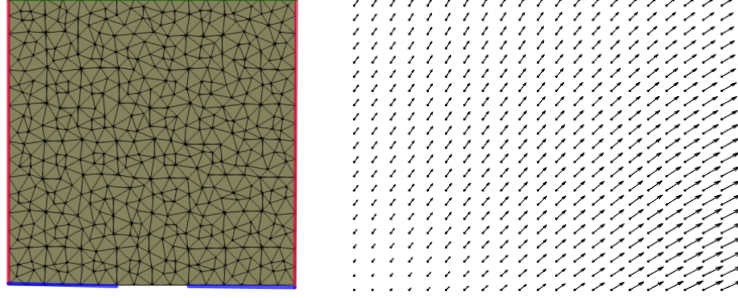


Figure 9: Test A: perturbed triangular mesh (left), and the distribution of the permeability field (right).

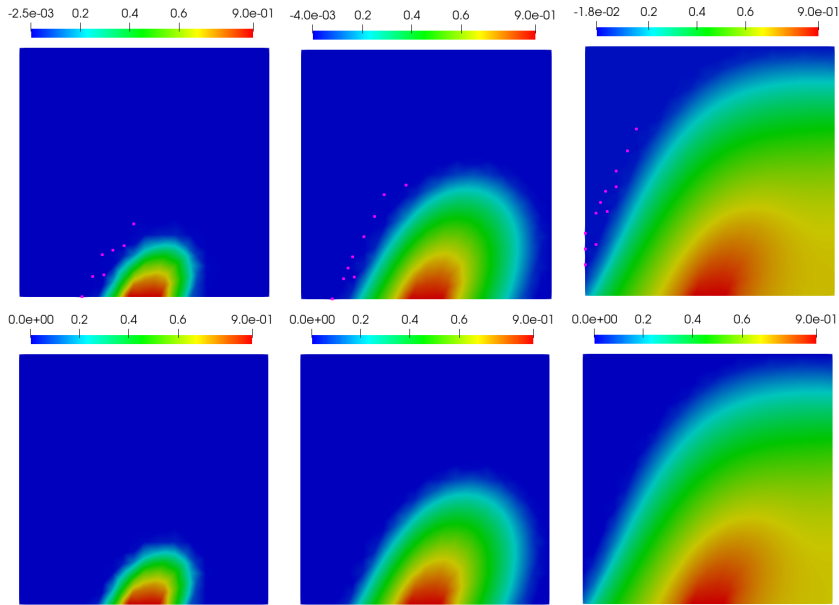


Figure 10: Test A: evolution of the CVFE solution (top), and of the WMFV solution (bottom) at $t_f = 0.03, 0.2, 1$. The magenta dots refer to the presence of undershoots.

includes two subvolumes that are less permeable. Indeed, $\Omega = \Omega_1 \cup \Omega_2 \cup \Omega_3$ where

$$\Omega_1 = [0.25, 1] \times [0.625, 0.75], \quad \Omega_3 = [0.25, 0.75] \times [0.25, 0.375], \quad \Omega_2 = (\Omega_1 \cup \Omega_3) \setminus \bar{\Omega}.$$

The permeability associated to each subset is given by

$$\Lambda_1 = 10^{-4}, \quad \Lambda_2 = \begin{pmatrix} \cos(\pi x) & -\sin(\pi x) \\ \sin(\pi x) & \cos(\pi x) \end{pmatrix} \begin{pmatrix} 1 & 0 \\ 0 & 0.01 \end{pmatrix} \begin{pmatrix} \cos(\pi x) & \sin(\pi x) \\ -\sin(\pi x) & \cos(\pi x) \end{pmatrix}, \quad \Lambda_3 = 10^{-3}.$$

The domain boundary is $\partial\Omega = \partial\Omega_{(1)}^D \cup \partial\Omega_{(2)}^D \cup \partial\Omega^N$ where

$$\partial\Omega_{(1)}^D = [0.9, 1] \times \{y = 0\} \cup \{x = 1\} \times [0, 0.1], \quad \partial\Omega_{(2)}^D = [0, 0.1] \times \{y = 1\}, \quad \partial\Omega^N = \partial\Omega \setminus (\partial\Omega_{(1)}^D \cup \partial\Omega_{(2)}^D).$$

This domain configuration is schematized in Figure 11. We set $u = 0.9$ on the part $\partial\Omega_{(1)}^D$, the free-flow on $\partial\Omega_{(2)}^D$ and the rest is impervious.

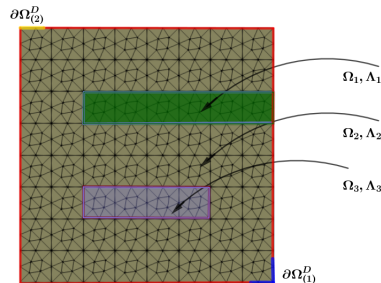


Figure 11: Test B : domain configuration.

The results are given Figures 12-13. The first plot corresponds to the CVFE solution at $t_f = 0.1$. It suffers from excessive undershoots such that their amplitude increases in time. After that moment, the Newton solver diverges and the CVFE algorithm breaks down. In the second plot, the WFMV scheme manages to recover an admissible solution which respects its physical ranges and resembles to the expected behavior.

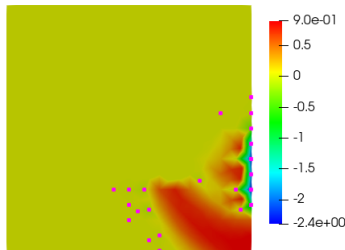


Figure 12: Test B: CVFE solution at $t_f = 0.1$.

6 Conclusion

In conclusion, we developed and analyzed a new numerical scheme based on the CVFE discretization for the approximation of parabolic equations. It is referred to as the weakly monotone finite volume scheme. As its name informs, the scheme yields numerical solution respecting some imposed physical ranges. For this purpose, we incorporated a nonlinear correction without changing the

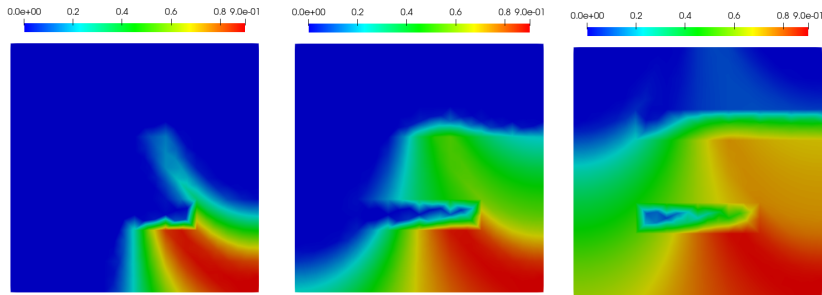


Figure 13: Test B: from left to right WMFV solution at $t_f = 1, 5, 15$ respectively.

stencil of the initial method. This enables the proof of the scheme’s stability consisting of the weak monotonicity and the energy estimates. As a consequence, the existence result was successfully proved. Numerical experiments yields promising results in terms of accuracy and robustness. Indeed, the WMFV scheme enjoys a similar accuracy as the CVFE version. It is also able to produce the expected numerical solution regardless the taken initial data or the imposed diffusion tensor. Thanks to these advantages, it was applied to simulate water diffusion in hygroscopic media of the wood type.

As a first perspective, we outlook to extend the current methodology to advanced systems modeling complex flows in hygroscopic media. Such a model can involve the convection term of type Darcy or Navier-Stokes. The second avenue is to combine the latter problem to an energy equation where the nonlinear coupling is more tough and hard to deal with.

Acknowledgments: Communauté urbaine du Grand Reims, Département de la Marne, Région Grand Est and European Union (FEDER Champagne-Ardenne 2014-2020) are acknowledged for their financial support to the Chair of Biotechnology of CentraleSupélec and the Centre Européen de Biotechnologie et de Bioéconomie (CEBB). The authors would like to thank the Moulay Ismaïl University for supporting partially this work (Project UMI 2018).

Conflicts of interest statement: the authors have no conflicts of interest to declare that are relevant to the content of this article.

References

- [1] I. Aavatsmark, T. Barkve, Ø. Bøe, and T. Mannseth. Discretization on non-orthogonal, quadrilateral grids for inhomogeneous, anisotropic media. *Journal of computational physics*, 127(1):2–14, 1996.
- [2] I. Aavatsmark, G. Eigestad, R. Klausen, M. Wheeler, and I. Yotov. Convergence of a symmetric MPFA method on quadrilateral grids. *Computational geosciences*, 11(4):333–345, 2007.

- [3] M. Afif and B. Amaziane. Convergence of finite volume schemes for a degenerate convection–diffusion equation arising in flow in porous media. *Computer Methods in Applied Mechanics and Engineering*, 191(46):5265–5286, 2002.
- [4] H. W. Alt and S. Luckhaus. Quasilinear elliptic-parabolic differential equations. *Math. z.*, 183(3):311–341, 1983.
- [5] B. Andreianov, F. Boyer, and F. Hubert. Discrete duality finite volume schemes for leray- lions- type elliptic problems on general 2D meshes. *Numerical Methods for Partial Differential Equations: An International Journal*, 23(1):145–195, 2007.
- [6] F. Boyer and F. Hubert. Finite volume method for 2D linear and nonlinear elliptic problems with discontinuities. *SIAM Journal on Numerical Analysis*, 46(6):3032–3070, 2008.
- [7] K. Brenner and R. Masson. Convergence of a vertex centred discretization of two-phase darcy flows on general meshes. *International Journal on Finite Volumes*, 10:1–37, 2013.
- [8] K. Brenner, R. Masson, and E. Quenjel. Vertex approximate gradient discretization preserving positivity for two-phase Darcy flows in heterogeneous porous media. *Journal of Computational Physics*, 409:109357, 2020.
- [9] E. Burman and A. Ern. Discrete maximum principle for Galerkin approximations of the Laplace operator on arbitrary meshes. *Comptes Rendus Mathématique*, 338(8):641–646, 2004.
- [10] C. Cancès, M. Cathala, and C. Le Potier. Monotone corrections for generic cell-centered finite volume approximations of anisotropic diffusion equations. *Numerische Mathematik*, 125(3):387–417, 2013.
- [11] C. Cancès and C. Guichard. Convergence of a nonlinear entropy diminishing control volume finite element scheme for solving anisotropic degenerate parabolic equations. *Mathematics of Computation*, 85(298):549–580, 2016.
- [12] B. Da Veiga, J. Droniou, and G. Manzini. A unified approach for handling convection terms in finite volumes and mimetic discretization methods for elliptic problems. *IMA Journal of Numerical Analysis*, 31(4):1357–1401, 2011.
- [13] N. Dahmen, J. Droniou, and F. Rogier. A cost-effective nonlinear extremum-preserving finite volume scheme for highly anisotropic diffusion on Cartesian grids, with application to radiation belt dynamics. *Journal of Computational Physics*, 463:111258, 2022.
- [14] K. Domelevo and P. Omnes. A finite volume method for the Laplace equation on almost arbitrary two-dimensional grids. *ESAIM: Mathematical Modelling and Numerical Analysis*, 39(6):1203–1249, 2005.
- [15] J. Droniou. Finite volume schemes for diffusion equations: introduction to and review of modern methods. *Mathematical Models and Methods in Applied Sciences*, 24(08):1575–1619, 2014.
- [16] J. Droniou, R. Eymard, T. Gallouët, C. Guichard, and R. Herbin. *The gradient discretisation method*, volume 82. Springer, 2018.

- [17] A. Ern and J.-L. Guermond. *Theory and practice of finite elements*, volume 159. Springer Science & Business Media, 2013.
- [18] L. C. Evans. *Partial differential equations*, volume 19. American Mathematical Soc., 2010.
- [19] R. Eymard, T. Gallouët, and R. Herbin. Finite volume methods. In *Handbook of Numerical Analysis*, volume 7, pages 713–1018. Elsevier, 2000.
- [20] R. Eymard, T. Gallouët, R. Herbin, M. Gutnic, and D. Hilhorst. Approximation by the finite volume method of an elliptic-parabolic equation arising in environmental studies. *Mathematical Models and Methods in Applied Sciences*, 11(09):1505–1528, 2001.
- [21] R. Eymard, T. Gallouët, D. Hilhorst, and Y. N. Slimane. Finite volumes and nonlinear diffusion equations. *ESAIM: Mathematical Modelling and Numerical Analysis*, 32(6):747–761, 1998.
- [22] R. Eymard, C. Guichard, and R. Herbin. Small-stencil 3D schemes for diffusive flows in porous media. *ESAIM: Mathematical Modelling and Numerical Analysis*, 46(2):265–290, 2012.
- [23] R. Eymard, D. Hilhorst, and M. Vohralík. A combined finite volume–nonconforming/mixed-hybrid finite element scheme for degenerate parabolic problems. *Numerische Mathematik*, 105(1):73–131, 2006.
- [24] P. A. Forsyth. A control volume finite element approach to NAPL groundwater contamination. *SIAM Journal on Scientific and Statistical Computing*, 12(5):1029–1057, 1991.
- [25] P. A. Forsyth and M. Kropinski. Monotonicity considerations for saturated–unsaturated subsurface flow. *SIAM Journal on Scientific Computing*, 18(5):1328–1354, 1997.
- [26] M. Ghilani, E. Quenjel, and M. Saad. Positive control volume finite element scheme for a degenerate compressible two-phase flow in anisotropic porous media. *Computational Geosciences*, 23(1):55–79, 2019.
- [27] M. Ghilani, M. Saad, et al. Positivity-preserving finite volume scheme for compressible two-phase flows in anisotropic porous media: The densities are depending on the physical pressures. *Journal of Computational Physics*, 407:109233, 2020.
- [28] C. Guichard and E. H. Quenjel. Weighted positive nonlinear finite volume method for dominated anisotropic diffusive equations. *Advances in Computational Mathematics*, 48(6):1–63, 2022.
- [29] R. Herbin and F. Hubert. Benchmark on discretization schemes for anisotropic diffusion problems on general grids. In R. Eymard and J.-M. Herard, editors, *Finite Volumes for Complex Applications V*, pages 659–692. Wiley, 2008.
- [30] F. Hermeline. A finite volume method for the approximation of diffusion operators on distorted meshes. *Journal of computational Physics*, 160(2):481–499, 2000.

- [31] M. Ibrahim, E. H. Quenjel, and M. Saad. Positive nonlinear DDFV scheme for a degenerate parabolic system describing chemotaxis. *Computers & Mathematics with Applications*, 80(12):2972–3003, 2020.
- [32] I. Kapyrin. A family of monotone methods for the numerical solution of three-dimensional diffusion problems on unstructured tetrahedral meshes. In *Doklady Mathematics*, volume 76(2), pages 734–738. Pleiades Publishing, 2007.
- [33] C. Le Potier. Correction non linéaire d'ordre 2 et principe du maximum pour la discrétisation d'opérateurs de diffusion. *Comptes Rendus Mathématique*, 352(11):947–952, 2014.
- [34] K. Lipnikov, D. Svyatskiy, and Y. Vassilevski. Interpolation-free monotone finite volume method for diffusion equations on polygonal meshes. *Journal of Computational Physics*, 228(3):703–716, 2009.
- [35] K. Lipnikov, D. Svyatskiy, and Y. Vassilevski. A monotone finite volume method for advection–diffusion equations on unstructured polygonal meshes. *Journal of Computational Physics*, 229(11):4017–4032, 2010.
- [36] F. Otto. L^1 -contraction and uniqueness for quasilinear elliptic–parabolic equations. *Journal of differential equations*, 131(1):20–38, 1996.
- [37] E. H. Quenjel. Enhanced positive vertex-centered finite volume scheme for anisotropic convection-diffusion equations. *ESAIM: Mathematical Modelling and Numerical Analysis*, 54(2):591–618, 2020.
- [38] E. H. Quenjel. Analysis of accurate and stable nonlinear finite volume scheme for anisotropic diffusion equations with drift on simplicial meshes. *Journal of Scientific Computing*, 88(3):1–26, 2021.
- [39] E. H. Quenjel. Positive Scharfetter-Gummel finite volume method for convection-diffusion equations on polygonal meshes. *Applied Mathematics and Computation*, 425:127071, 2022.
- [40] E. H. Quenjel and P. Perré. Computation of the effective thermal conductivity from 3D real morphologies of wood. *Heat and Mass Transfer*, 58:219–2206, 2022.
- [41] E. H. Quenjel, M. Saad, M. Ghilani, and M. Bessemoulin-Chatard. Convergence of a positive nonlinear DDFV scheme for degenerate parabolic equations. *Calcolo*, 57(2):1–38, 2020.
- [42] Z. Sheng and G. Yuan. The finite volume scheme preserving extremum principle for diffusion equations on polygonal meshes. *Journal of Computational Physics*, 230(7):2588–2604, 2011.
- [43] G. Yuan and Z. Sheng. Monotone finite volume schemes for diffusion equations on polygonal meshes. *Journal of computational physics*, 227(12):6288–6312, 2008.